Journal of Biomedical Optics

BiomedicalOptics.SPIEDigitalLibrary.org

In vivo visualization of prostate brachytherapy seeds with photoacoustic imaging

Muyinatu A. Lediju Bell
Nathanael P. Kuo
Danny Y. Song
Jin U. Kang
Emad M. Boctor

SPIE.

In vivo visualization of prostate brachytherapy seeds with photoacoustic imaging

Muyinatu A. Lediju Bell,[a,*] Nathanael P. Kuo,[b,c] Danny Y. Song,[d] Jin U. Kang,[c] and Emad M. Boctor[a,c,e,*]
[a]Johns Hopkins University, CISST Engineering Research Center, Baltimore, Maryland 21218, United States
[b]Johns Hopkins University, Department of Biomedical Engineering, Baltimore, Maryland 21218, United States
[c]Johns Hopkins University, Department of Electrical and Computer Engineering, Baltimore, Maryland 21218, United States
[d]Johns Hopkins University School of Medicine, Department of Radiation Oncology and Molecular Radiation Sciences, Baltimore, Maryland 21205, United States
[e]Johns Hopkins University, School of Medicine, Department of Radiology, Baltimore, Maryland 21205, United States

Abstract. We conducted a canine study to investigate the *in vivo* feasibility of photoacoustic imaging for intraoperative updates to brachytherapy treatment plans. A fiber coupled to a 1064-nm Nd:YAG laser was inserted into high-dose-rate brachytherapy needles, which diffused light spherically. These needles were inserted through the perineum into the prostate for interstitial light delivery and the resulting acoustic waves were detected with a transrectal ultrasound probe. Postoperative computed tomography images and *ex vivo* photoacoustic images confirmed seed locations. Limitations with insufficient light delivery were mitigated with short-lag spatial coherence (SLSC) beamforming, providing a 10–20 dB contrast improvement over delay-and-sum (DAS) beamforming for pulse energies ranging from 6.8 to 10.5 mJ with a fiber-seed distance as large as 9.5 mm. For the same distance and the same range of energy densities, signal-to-noise ratios (SNRs) were similar while the contrast-to-noise ratio (CNR) was higher in SLSC compared to DAS images. Challenges included visualization of signals associated with the interstitial fiber tip and acoustic reverberations between seeds separated by ≤2 mm. Results provide insights into the potential for clinical translation to humans. [DOI: 10.1117/1.JBO.19.12.126011]

Keywords: brachytherapy; dynamic dosimetry; intraoperative treatment planning; image-guided intervention; optoacoustic imaging.

Paper 140156PRR received Mar. 7, 2014; revised manuscript received Sep. 2, 2014; accepted for publication Oct. 13, 2014; published online Dec. 22, 2014.

1 Introduction

Brachytherapy is a popular treatment option for prostate cancer, administered by permanently implanting approximately 50 to 120 seeds according to a defined treatment plan.[1,2] The seeds are filled with radioactive isotopes, typically iodine-125 or palladium-103, and each treatment plan is designed to maximize the dose to cancerous regions while sparing healthy tissue.[3,4] Although prostate brachytherapy has excellent 5- to 10-year treatment outcomes,[5–7] complications typically arise when there is a mismatch between the planned and delivered doses caused by factors such as seed migration, prostate motion, edema, or surgeon-dependent implantation errors.[8,9] The potential for a mismatch between planned and delivered doses can be avoided with a treatment planning approach that allows dynamic, intraoperative updates to the original treatment plan.[6,10]

The first step toward intraoperative treatment planning is real-time seed localization, which is currently performed with transrectal ultrasound (TRUS) imaging.[11,12] Yet, seeds are often difficult to locate with ultrasound due to factors such as the small size of the seeds and the presence of calcifications that may be mistaken for seeds. In addition, inherent acoustic properties or artifacts (e.g., shadowing, reverberation, specular reflections) present challenges for seed localization.[13–15] Thus, postoperative computed tomography (CT) images are conventionally employed to confirm seed locations and determine if alternative forms of treatment (e.g., external beam therapy) are needed to compensate for underdosed regions of the prostate.[16] This approach increases the risks associated with radiation exposure and does not address complications that may occur with overdosing healthy tissues, such as urinary incontinence, rectal damage, or erectile dysfunction.[4] It is less likely that over- or under-dosage will occur if seeds are better visualized during an operation.

Photoacoustic imaging has the potential to complement ultrasound detection of brachytherapy seeds and to overcome current limitations with intraoperative seed visualization.[17–19] It is based on light transmission and the optical absorption of a target, which subsequently undergoes thermoelastic expansion and generates sound waves that are detectable with conventional ultrasound transducers.[20] Thus, the main additional hardware required to introduce photoacoustic imaging into a clinical brachytherapy suite is a laser system that transmits nanosecond light pulses. The light is absorbed by the seeds and the resulting sound waves may be detected with the same TRUS probe that is used for seed and needle visualization. Excellent seed contrast is expected with photoacoustic imaging because the optical absorption of the seeds is significantly larger than that of the surrounding tissue.[18]

Several researchers previously assessed the feasibility of seed visualization with photoacoustic imaging of phantoms and *ex vivo* data, noting properties such as sensitivity to seed orientation,[18,21] sufficient light penetration in prostatic tissue,[18] isolation of seed-related signals from blood-related signals at a laser wavelength of 1064 nm,[17] and enhanced seed contrast

*Address all correspondence to: Muyinatu A. Lediju Bell, E-mail: muyinatu.ledijubell@jhu.edu; Emad M. Boctor, E-mail: eboctor1@jhu.edu

with a highly absorptive coating.[22] In addition, our previous work introduced an interstitial, transperineal light delivery method and short-lag spatial coherence (SLSC) beamforming to increase seed contrast and extend the effective penetration depth in the presence of minimal laser fluence.[23] The SLSC beamformer, which was initially developed for ultrasound imaging,[24–26] was applied to line, spherical, and transcranial photoacoustic targets with similarly promising results.[27,28]

This paper builds on previous work by translating a customized photoacoustic system to an animal operating room and testing the interstitial transperineal light delivery method on two canine prostates in the presence of living blood, proteins, and other endogenous chromophores. The utility of the SLSC beamformer is also explored for these *in vivo* conditions. To the authors' knowledge, this work is the first to demonstrate the *in vivo* feasibility of visualizing prostate brachytherapy seeds with combined photoacoustic and ultrasound images.

2 Methods and Materials

2.1 *Imaging Equipment*

The ultrasound equipment consisted of three main components manufactured by Ultrasonix (Richmond, BC, Canada). A SonixTouch ultrasound scanner was connected to a transrectal ultrasound probe with linear (BPL9-5/55) and curvilinear (BPC8-4/10) arrays containing 128 elements each with bandwidths of 5 to 9 and 4 to 8 MHz, respectively. This system acquired beamformed pulse-echo radiofrequency (RF) ultrasound data with transmit frequencies of 6.6 MHz with the linear array and 6.0 MHz with the curvilinear array.

For photoacoustic imaging, one of the transducer ports on the ultrasound scanner was connected to a data acquisition unit (Ultrasonix SonixDAQ) to access raw prebeamformed RF data with the linear and curvilinear arrays of the TRUS probe at a sampling rate of 40 MHz. The SonixDAQ was triggered by the flashlamp output signal of a Phocus neodymium-doped yttrium aluminum garnet (Nd:YAG) laser manufactured by Quantel (Bozeman, Montana) with an optical parametric oscillator installed by Opotek (Carlsbad, California). The primary wavelength of the Nd:YAG laser, 1064 nm, was used to distinguish photoacoustic signals from blood.[17] The laser repetition rate was 10 Hz with a 5-ns pulse duration, and the laser beam was air-coupled into a 1-mm core diameter optical fiber. The laser and all optical components were secured on a portable optical table (Thorlabs, New Jersey) for mobility in the operating room. The optical table was enclosed in a black box with a small hole to expose the optical fiber. Five frames of RF data were recorded for each acquisition.

A Philips (Andover, Massachusetts) XperCT scanner was utilized to acquire postoperative CT images of the canine prostate. Each image in the volume stack was 384×384 pixels with approximately 0.5 mm spacing between pixels.

2.2 *In Vivo Experiment*

Two dogs were prepared for a prostate brachytherapy procedure approved by the Johns Hopkins Animal Care and Use Committee (Protocol #DO13M143). After sedation and intravenous induction, anesthesia was maintained with continuous inhalation of 1% to 3% isoflurane. The perineum was shaved and a urinary catheter was inserted. The dog was positioned supine with its legs immobilized, and was continuously monitored throughout the procedure.

A portable Nucletron prostate stepper (Veenendaal, The Netherlands) held the transrectal ultrasound probe, as shown in Fig. 1(a). A Nucletron prostate stepper template for brachytherapy with a square grid of holes, equally spaced by 5 mm in the horizontal and vertical directions, was attached to the stepper. The grid was then aligned with the perineum and the stepper was locked in place. After protecting the transrectal ultrasound probe with a sanitized latex probe cover, it was inserted in the rectum to visualize the prostate.

Nonradioactive, titanium, cylindrical brachytherapy seeds with a length of 4.5 mm and outer diameter of 0.8 mm (TheraSeed, Theragenics Corporation, Buford, Georgia) were painted with black India ink to increase optical absorption, an approach that was similarly implemented by Pan et al.[22] This is a reasonable modification for seeds purposely designed for photoacoustic imaging, and similar enhancement coatings are common in brachytherapy.[29] Previous work describes that metals[18,30,31] and India ink[32] have orders of magnitude higher optical absorption than prostatic tissue and other endogenous chromophores. The optical absorption of the black coating likely adds to that of the metal[33,34] to generate a photoacoustic response from the seeds.

A standard 18G brachytherapy needle (Bard, Brachystar, Covington, Georgia), consisting of a hollow outer cannula and removable inner stylet, was inserted through one of the holes in the template, through the perineum, and into the prostate under transrectal ultrasound guidance. Needle placement was confirmed by rotating the ultrasound probe to obtain several views of the needle tip. A seed was deposited into the prostate by first removing the stylet of the needle, manually inserting the seed through the cannula, and pushing the seed into the tissue with the stylet. This process was repeated for each implanted seed.

Interstitial light delivery was facilitated by a hollow, plastic, high-dose-rate (HDR) brachytherapy needle of inner diameter 1.5 mm and outer diameter 2.0 mm (ProGuide 6F sharp, manufactured by Nucletron, Veenendaal, The Netherlands). A photograph of this needle is shown in Fig. 1(b) with dimensions of the outer diameter and slant height illustrated in Fig. 1(c). The needle acted as a light diffuser when the fiber was inserted and light was emitted through the fiber tip enabling spherical light delivery within at least 1 cm of the fiber tip (as estimated from the geometry of the light profile shown in Fig. 1(d), which was obtained with a 635-nm laser wavelength). We refer to this HDR needle as a light diffusing sheath throughout the manuscript. The light diffusing sheath was inserted through the template grid and perineum with the aid of a stiff guide needle that is typically used in HDR brachytherapy procedures. The guide needle was then removed and replaced with the 1-mm core diameter optical fiber. The light diffusing sheath containing the optical fiber was positioned parallel to the seeds at distances of approximately 3 to 11 mm from the seeds. Throughout this paper, the seeds and light diffusing sheaths are numbered in order of insertion for each dog and the location of the fiber tip inside the sheath is denoted as a red dot in the schematic diagrams that accompany each *in vivo* result. Sheaths that are in the same plane as the schematic diagrams are shown with solid lines, while out-of-plane sheaths are shown with dashed lines.

For the first dog, photoacoustic imaging was performed as the energy transmitted through the sheath tip was varied from 5.3 to 10.5 mJ per pulse. The second dog was imaged with

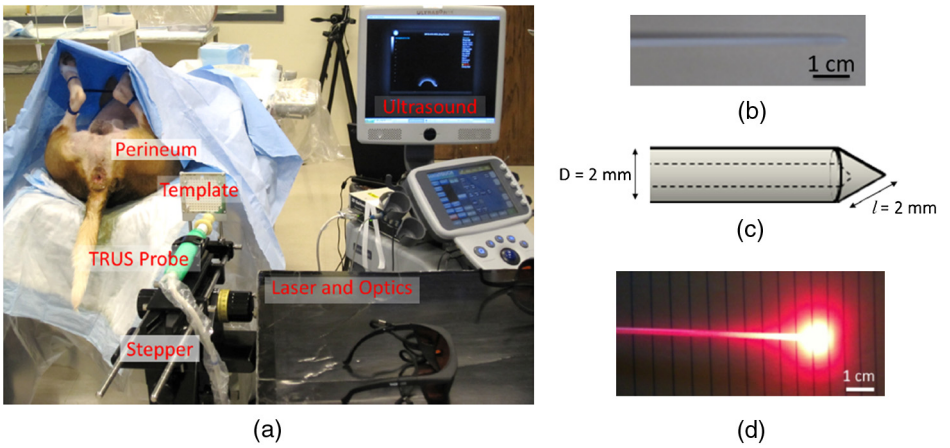

Fig. 1 (a) Experimental equipment for *in vivo* imaging of the canine prostate. (b) Photograph of a high-dose-rate (HDR) brachytherapy needle that acted as a light diffuser. (c) Geometry of the HDR needle tip. (d) Light was diffused within approximately 1 to 2 cm surrounding the fiber tip by inserting the fiber into the HDR needle.

an average energy of 5.6 mJ at the sheath tip. The surface area used to estimate energy densities was based on a conical sheath tip approximation, given the measured cone slant height ($l = 2$ mm), base diameter ($D = 2$ mm), and the equation for the surface area of a cone: area $= \pi(D/2)l$. Thus, the surface area of the sheath tip was 0.063 cm^2, and the corresponding energy densities at the fiber tip are reported in Table 1.

The energy densities at individual seed locations depend on several optical parameters (e.g., absorption and reduced scattering coefficients, which can range from 0.03 to 0.27 cm^{-1} and 6.3 to 17.6 cm^{-1}, respectively, at a 1064-nm laser wavelength in canine prostates[35–37]). Rastegar et al.[38] performed Monte Carlo simulations to demonstrate that the light intensity decreases by 47% to 93% at distances of 3 to 10 mm from the light source with absorption and scattering coefficients of 0.37 and 8.2 cm^{-1}, respectively. Although the light distribution within the prostate is quite complex,[39] the energy density measurements at the fiber tip are generally expected to decrease by a similar percentage with distance from the light source, and seeds farthest from the fiber tip are expected to experience the least fluence.

Pulse-echo RF ultrasound data were acquired with each probe adjustment for photoacoustic imaging. CT images were acquired after the operation to confirm seed locations. Additional markers implanted in the first dog for an unrelated study[40] were present in a few of the ultrasound and CT images.

2.3 *Ex Vivo Study*

The first dog was sacrificed after the brachytherapy procedure and its prostate was excised and transported in saline. Approximately 1 week after excision, a 14 F (4.7-mm outer diameter) urinary catheter was inserted into the prostate and the prostate and catheter were embedded in gelatin to confirm photoacoustic visualization of the implanted brachytherapy seeds. To maintain the structural integrity of the prostate, the optical fiber was placed inside the urinary catheter for transurethral light delivery to the implanted seeds. A channel was drilled in the layer of gelatin located below the prostate to correspond with the anatomical relationship between the prostate and rectum. The transrectal probe, held by the Nucletron stepper, was inserted into this channel. Photoacoustic and ultrasound images of the prostate and implanted brachytherapy seeds were acquired with this setup.

2.4 *Image Formation*

A conventional delay-and-sum (DAS) beamformer and a coherence-based SLSC beamformer were applied to the received photoacoustic signals. Received signal time delays were calculated with 33-element subapertures for the DAS and SLSC photoacoustic images. Hanning apodization was applied to the delayed signals for DAS beamforming. No apodization was applied for SLSC beamforming.

SLSC photoacoustic images were calculated using the following equations for the normalized spatial correlation of received signals, $\hat{R}$, and the short-lag spatial coherence, R_{sl}:[24,41]

$$\hat{R}(m) = \frac{1}{N-m}\sum_{i=1}^{N-m}\frac{\sum_{n=n_1}^{n_2} s_i(n)s_{i+m}(n)}{\sqrt{\sum_{n=n_1}^{n_2} s_i^2(n)\sum_{n=n_1}^{n_2} s_{i+m}^2(n)}}, \quad (1)$$

$$R_{\mathrm{sl}} = \sum_{m=1}^{M}\hat{R}(m), \quad (2)$$

where m is the distance (i.e., lag) between the two elements on the receive aperture in units of number of elements, N is the total number of elements in the receive aperture, $s_i(n)$ is the

Table 1 Energies measured at the tip of the fiber surrounded by the light-diffusing sheath and corresponding energy densities.

Energy per pulse (mJ)	5.3	5.6	6.0	6.8	7.7	9.0	9.9	10.5
Energy density (mJ/cm^2)	84	89	95	108	123	143	158	167

time-delayed, zero-mean signal received by the ith transducer element, n is the sample depth in units of samples, and M is the number of lags included in the short-lag sum. The value of $n_2 - n_1$ was equivalent to the smallest wavelength within the bandwidth of the linear array (i.e., 0.308 mm). The value of M was adjusted to optimize seed visualization in each imaging scenario. Our previous publication[23] indicates that curvilinear images require higher values of M to preserve the point-like seed resolution, while lower values of M were best for visualizing the long axis of the seeds with the linear array.

Beamformed ultrasound and photoacoustic data were envelope detected, normalized to the brightest image pixel, and log compressed. In addition, images acquired with the curvilinear array were scan converted. *Ex vivo* and *in vivo* photoacoustic images were displayed with 15 and 20 dB dynamic ranges, respectively. Unless otherwise stated, no frame averaging was applied to display the images. All image processing was performed with MATLAB® software (The MathWorks, Inc., Natick, Massachusetts).

2.5 *Image Quality Metrics*

The contrast, contrast-to-noise ratio (CNR), and signal-to-noise ratio (SNR) of signals in the photoacoustic images were calculated using the following equations:

$$\text{Contrast} = 20\log_{10}\left(\frac{S_i}{S_o}\right), \tag{3}$$

$$\text{CNR} = \frac{|S_i - S_o|}{\sigma_o}, \tag{4}$$

$$\text{SNR} = \frac{S_i}{\sigma_o}, \tag{5}$$

where S_i and S_o are the means of the image data within regions of interest (ROIs) located inside and outside a signal of interest (i.e., a brachytherapy seed or photoacoustic artifact), respectively, and σ_o is the standard deviation of the data within the ROI located outside of the signal. In the context of this paper, an artifact is defined as any photoacoustic signal that is not a seed.

Rectangular ROIs surrounding the maximum signal from the seed or artifact were manually selected, and a matching ROI at the same depth and with the same size was automatically created, with its left or right edge located at a fixed lateral position from the signal. The fixed lateral position was the same in paired SLSC and DAS photoacoustic images. The average ROI size $\pm$ one standard deviation was 0.7 ± 0.2 mm (axial) $\times$ 2.5 ± 1.1 mm (lateral). The lateral separation between the signal and noise ROIs was at least 5 mm.

The three-dimensional (3-D) locations of the implanted seeds were identified in the post operative CT images. The relative distance between seeds was measured in photoacoustic and ultrasound images for comparison with CT images. Ultrasound and photoacoustic image analyses were performed with MATLAB software, and CT image analyses were performed with ImageJ software.[42]

3 Results

3.1 *In Vivo Seed Visualization*

Figure 2(a) shows the orientation of three seeds implanted in the first canine prostate and their relationship to the TRUS probe and the light source (i.e., the fiber inserted into the light-diffusing sheath). Seed #1 is located closest to the probe. The distance between the fiber tip and the closest edge of seed #1 was less than 1 mm in the **x** direction of Fig. 2(a), as indicated by the red dot in the out-of-plane sheath (dashed lines).

The diameters of three implanted brachytherapy seeds were visible in axial slices of the postoperative CT image, as demonstrated in Fig. 2(b). The location of the transrectal ultrasound probe at the time of the experiment is indicated with the blue circle. This location was confirmed with a postoperative CT image acquired with the probe left in place (not shown because the image contained streak artifacts caused by the metal components of the probe, which obscured seed locations). The linear array of the TRUS probe was rotated to the direction shown in Fig. 2(b) to visualize the three seeds in ultrasound and photoacoustic images.

The long axes of the seeds are shown in Fig. 2(c), with arrows indicating seeds #1 to 3. It is difficult to visualize these seeds in the ultrasound image due to their small size and limited acoustic contrast with the prostatic tissue. In addition, the location of seed #3 might be confused with the reverberation artifact that appears above this seed, which does not agree with the 3.8-mm distance between seeds #2 and 3 measured in the postoperative CT image.

A co-registered photoacoustic image created with the DAS beamformer is overlaid on the ultrasound image in a yellow–red color scale in Fig. 2(d). Two of the three seeds are better visualized in the photoacoustic image (seeds #1 and 2), in addition to an artifact that does not correlate with the location of any implanted seeds (unlabeled white arrow). Seed #3 is poorly visualized in the expected location, but it can also be mistaken for a photoacoustic artifact. There is an additional fainter signal that corresponds with the location of the out-of-plane fiber (red arrow).

One approach to enhance the visualization of seed #3 is to implement SLSC beamforming, as shown in Fig. 2(e), with a short-lag value of $M = 4$. The seeds in Figs. 2(d) and 2(e) are shown in Fig. 2(f) as the energy density at the fiber tip was varied from 84 to 167 mJ/cm^2. Seed #3 is visible in the SLSC images ($M = 1$) for energy densities ranging 108 to 167 mJ/cm^2. However, seed #3 is not visible at lower energies because the fluence is probably not sufficient to generate a photoacoustic effect. In the image taken with 167 mJ/cm^2 laser fluence, note that the fiber-related artifact (denoted as "A") is more prominent than the adjacent seed #1.

Contrast was measured as a function of energy density at the fiber tip for these three seeds and the two artifacts, as shown in Figs. 3(a) and 3(d) for DAS and SLSC images, respectively. The seed contrast generally increases with increasing energy in DAS images, and the local minima may be caused by involuntary prostate motion or peristalsis. Note that the fiber-related artifact has higher contrast than seed #3, and thresholding the photoacoustic image to remove this artifact in the DAS image would also remove the low-contrast seed signal. The additional artifact [unlabeled white arrows in Figs. 2(d) and 2(e)] has the highest contrast. These artifacts are investigated in more detail in Secs. 3.3 and 3.4.

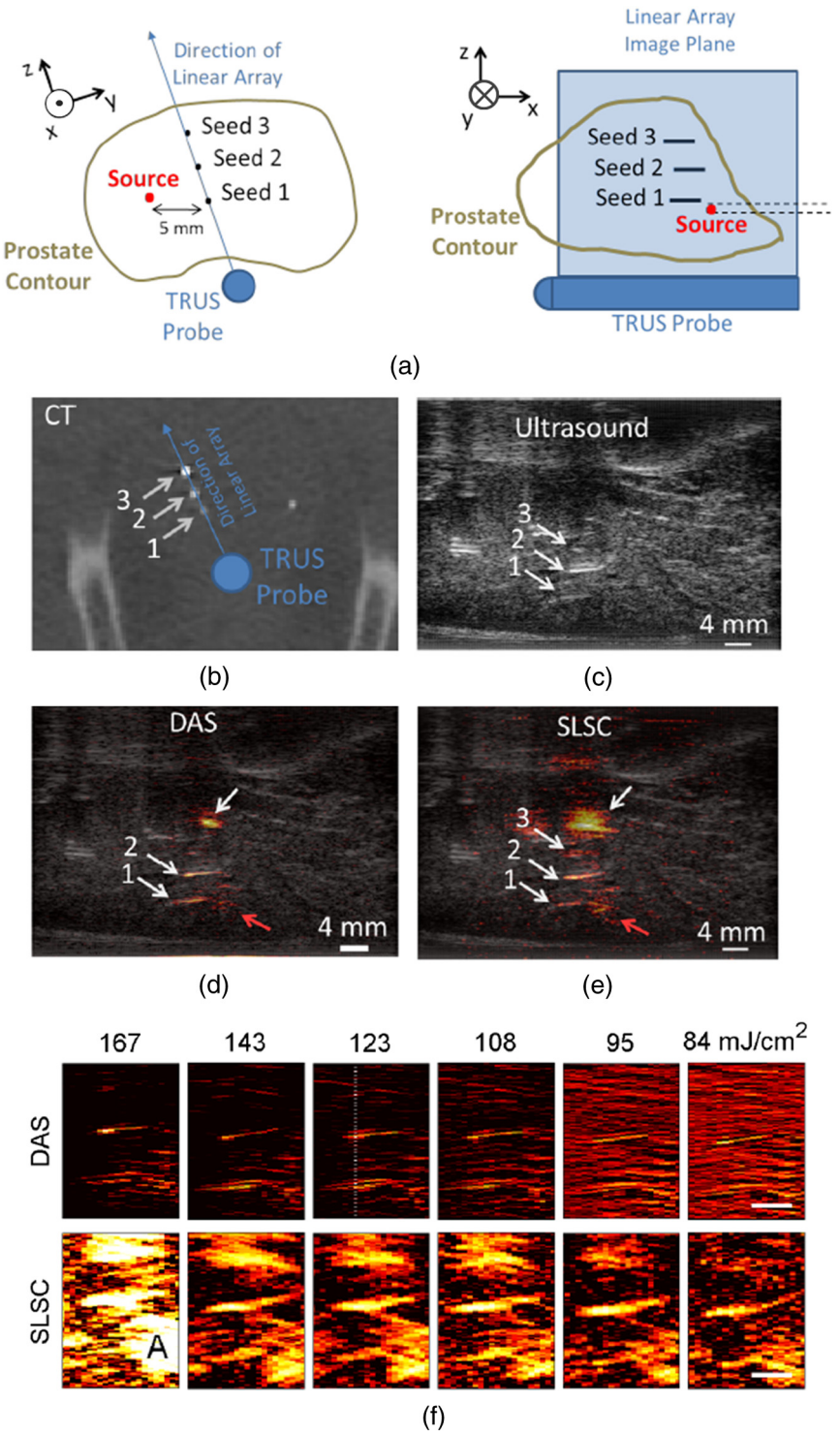

Fig. 2 (a) Schematic diagrams of three implanted seeds relative to the light source and transrectal ultrasound (TRUS) probe (not drawn to scale). Visualization of three brachytherapy seeds with (b) postoperative computed tomography (CT) and (c) conventional ultrasound imaging. Photoacoustic images created with the (d) delay-and-sum (DAS) and (e) short-lag spatial coherence (SLSC) beamformers overlaid on the ultrasound image in a yellow–red color scale (123 mJ/cm^2 energy density at the fiber tip). Unlabeled arrows point to photoacoustic artifacts. (f) DAS and SLSC photoacoustic images as the energy density at the fiber tip was varied between 84 and 167 mJ/cm^2. These images were averaged over five frames. The faint vertical line in the DAS image acquired with 123 mJ/cm^2 indicates the lateral position of the line plots in Fig. 5 and the "A" indicates an artifact. The scale bar is 4 mm.

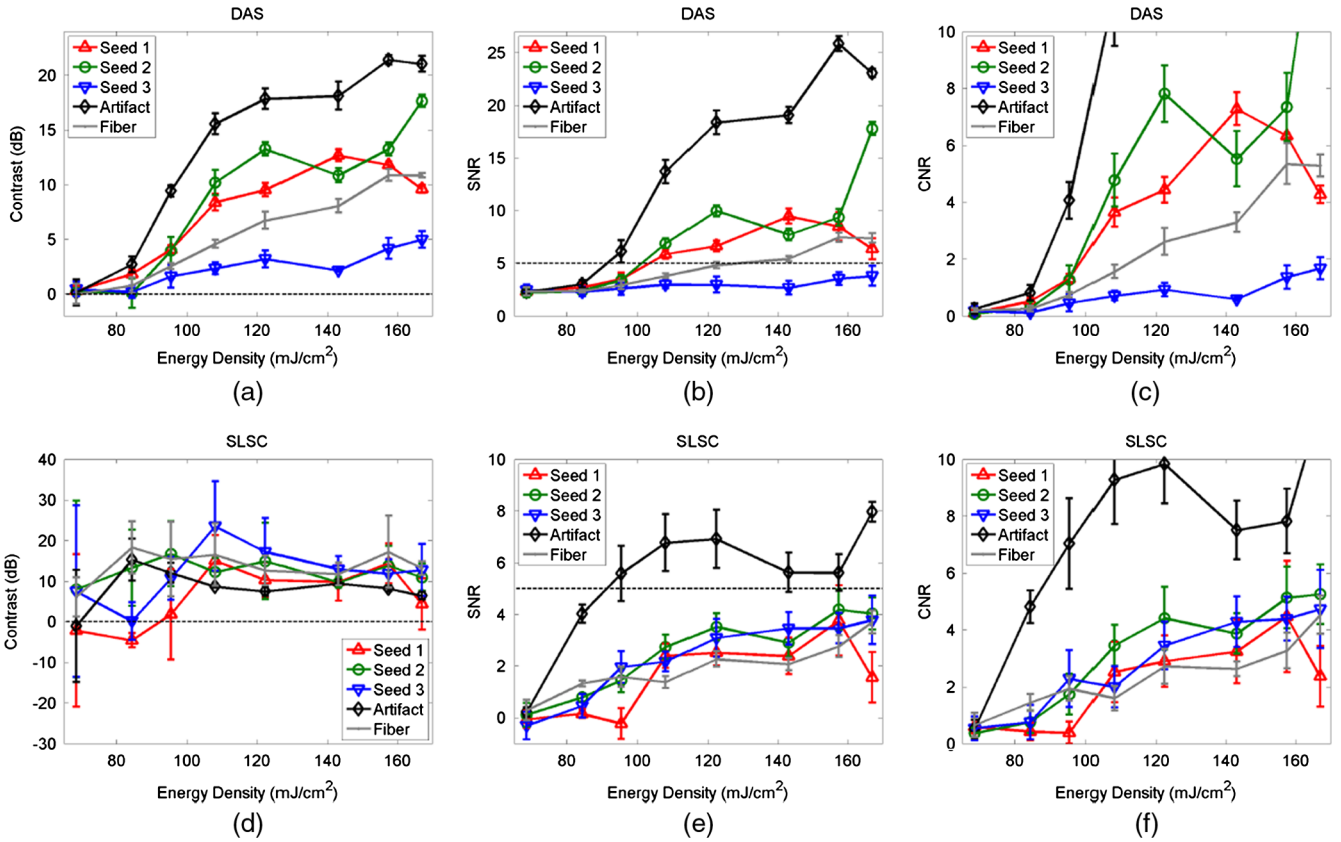

Fig. 3 Contrast, signal-to-noise ratio (SNR), and contrast-to-noise ratio (CNR) of the three seeds and two artifacts in Figs. 2(d) and 2(e), measured in (a,b,c) DAS and (d,e,f) SLSC images, respectively, as a function of energy density at the sheath tip surrounding the optical fiber. Horizontal reference lines were added to assist with comparisons between plots that are not shown with the same scale.

In SLSC images, average contrast values near or below 0 dB indicate that the seeds were not visible in the photoacoustic image. The SLSC contrast measurements peak when signals transition from barely visible or not visible to visible. This peak occurs at 84 mJ/cm^2 for the two artifacts and 108 mJ/cm^2 for seeds #1 and 3, while seed #2 appears to be visible for all energies. Beyond these transition points, the average contrast was 9 to 24 dB, and seed #1 lost visibility at 167 mJ/cm^2. In addition, the contrast of artifacts was similar to that of the seeds despite the largely different amplitudes.

The corresponding SNR measurements in Figs. 3(b) and 3(e) indicate that DAS images have similar or better SNR than SLSC images over the range of energies and light–fiber distances investigated. A reference line was drawn at an SNR of 5 to assist with comparisons between these two plots.

The corresponding CNR measurements in Figs. 3(c) and 3(f) are displayed with the same scale. CNR is better at larger energies for seed #3 in SLSC images compared to DAS images. Otherwise, the CNR of the DAS images outperforms that of the SLSC images.

3.2 *Ex Vivo Validation*

After embedding the excised canine prostate in gelatin, the TRUS probe was oriented to visualize the three seeds shown in Fig. 2(a). Linear and curvilinear B-mode images are shown in Figs. 4(a) and 4(d), respectively. The arrows point to the three seeds in the linear image, which correspond with the known seed locations. The erroneous seed visualized *in vivo* is not present in this image. Only two of the three seeds were visible in the curvilinear B-mode image. To acquire photoacoustic images, a bare fiber was placed in the urinary catheter at a 3-D distance of approximately 12 mm from seed #2 [i.e., 6 mm laterally from the tip of seed #2 in Fig. 4(a) and approximately 10 mm radially from seed #2 in Fig. 4(d)]. The average energy per pulse measured at the tip of the fiber was 16.7 mJ.

The linear photoacoustic image of the seeds was displayed with DAS and SLSC ($M = 4$) beamforming and overlaid on the co-registered B-mode image, as shown in Figs. 4(b) and 4(c), respectively. The three seeds appear angled rather than horizontal, possibly because the prostate is rotated relative to its *in vivo* orientation. The curvilinear photoacoustic images shown in Figs. 4(e) and 4(f) were formed with the DAS and SLSC ($M = 10$) beamformers, respectively. Only two of the three seeds are visible in the curvilinear B-mode image, while all three seeds were visualized with photoacoustic imaging. Note that in addition to photoacoustic signals from the three brachytherapy seeds, photoacoustic artifacts that do not correlate with any of the known seed locations are present. The artifact is more prominent in the SLSC image.

Figure 5 shows a CT line plot along the direction of the linear array illustrated in Fig. 2(a), compared to line plots though the seeds in the *in vivo* and *ex vivo* photoacoustic images acquired

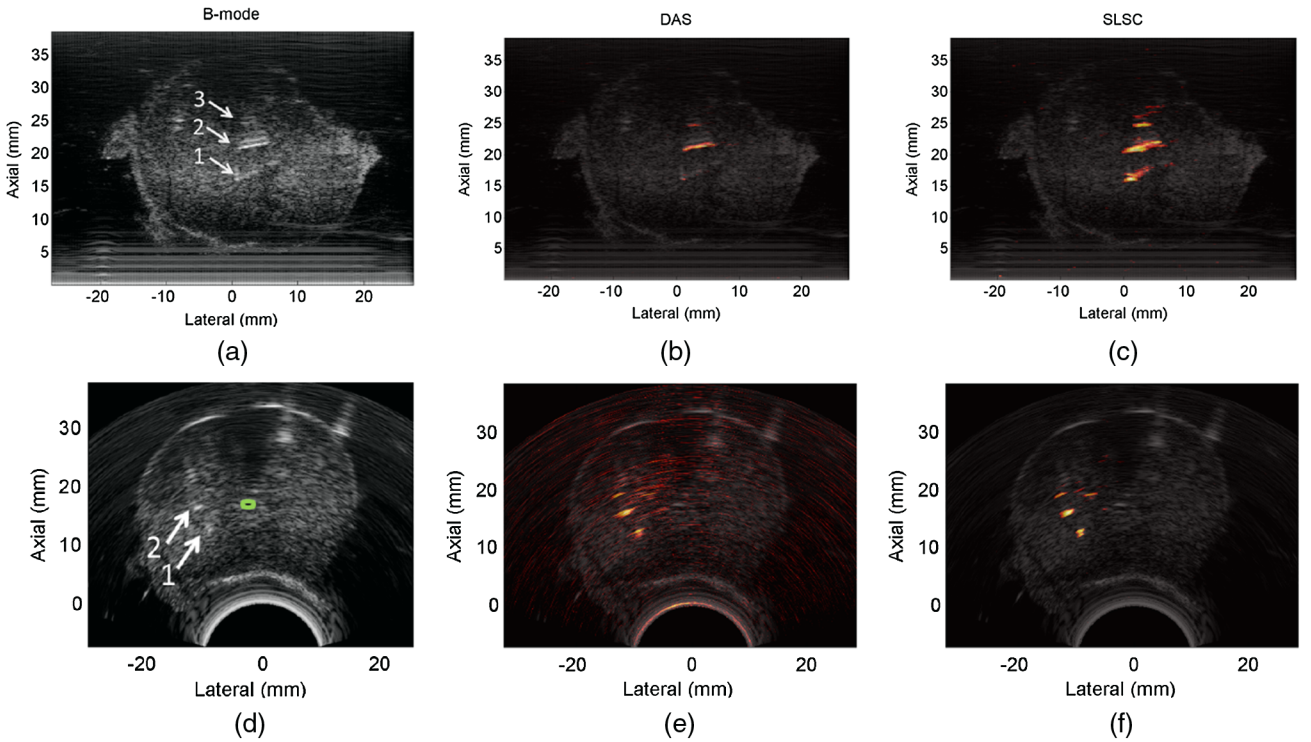

Fig. 4 (a) Linear and (d) curvilinear ultrasound images of the *ex vivo* prostate implanted with the three seeds shown in Fig. 2. The arrows point to the visible seeds in the B-mode images, while the urethra is contoured in green. (b,e) Corresponding linear and curvilinear DAS photoacoustic images of the seeds overlaid on the ultrasound images. (c,f) Corresponding linear and curvilinear SLSC photoacoustic images overlaid on the ultrasound images. A transurethral light delivery method was utilized to obtain the photoacoustic images.

with the linear array [Figs. 2(f) and 4(c), respectively], along the lateral position indicated by the faint vertical line in Fig. 2(f) (123 mJ/cm^2). The axial distance between the centers of seeds #1 and 2 was 3.7 mm in the *ex vivo* photoacoustic image, a difference of less than 0.1 mm from the 3.8 mm measured in the *in vivo* DAS and SLSC images. Both measurements agree with the 3.7 mm spacing between seeds #1 and 2 measured in the CT image shown in Fig. 2(a). The axial distance between seeds #2 and 3 is 3.8 mm in the *ex vivo* photoacoustic

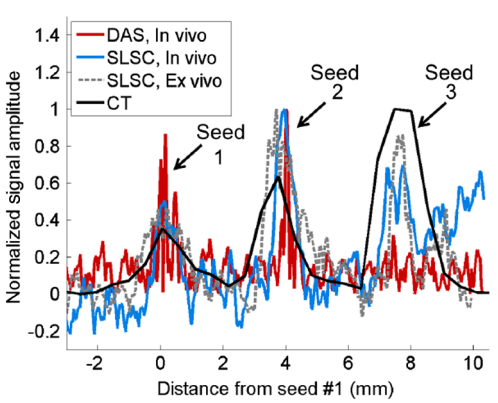

Fig. 5 Comparison of signal amplitudes along the direction of the linear array, taken from line plots along the seeds in the CT image [Fig. 2(b)], *in vivo* images [Fig. 2(f), 123 mJ/cm^2], and *ex vivo* image [Fig. 4(c)]. The distance measurements are aligned with the first peak, which corresponds with the location of seed #1. The signal amplitudes are normalized to the maximum signal in each line plot.

image, which is in excellent agreement with the 3.7 and 3.8 mm distances measured in the *in vivo* SLSC image and postoperative CT image, respectively. These distances were used to estimate that seed #2 was located approximately 6.5 mm from the interstitial transperineal light source, while seed #3 was located approximately 9.5 mm from the light source, as summarized in Table 2.

3.3 *Fiber-Related Artifacts*

A second dog was imaged to further investigate some of the challenges observed with photoacoustic imaging of prostate brachytherapy seeds. A light diffusing sheath was inserted into this second canine prostate before implanting any seeds. The ultrasound probe was directed toward the fiber inside the sheath (Source 1), as illustrated in Fig. 6(a) [with the direction of the linear array labeled as (b)]. The resulting linear photoacoustic image of the sheath tip and the corresponding curvilinear image are shown in Figs. 6(b) and 6(c), respectively.

After seeds #4 and 5 were inserted, the linear array was rotated toward these seeds, away from the tip of Source 1 [direction denoted with the (d) in Fig. 6(a)], and a similar, more diffuse artifact that corresponds to a projection of the fiber tip onto the image plane appeared, as shown in Fig. 6(d). This artifact is located at an axial distance of 15 to 20 mm from the probe. When the curvilinear array was translated superior to the fiber tip, the artifact related to the same fiber is located at a similar axial distance from the probe, as shown in Fig. 6(e).

Thus, the size and appearance of this fiber-related artifact depend on the distance of the imaging plane from the fiber

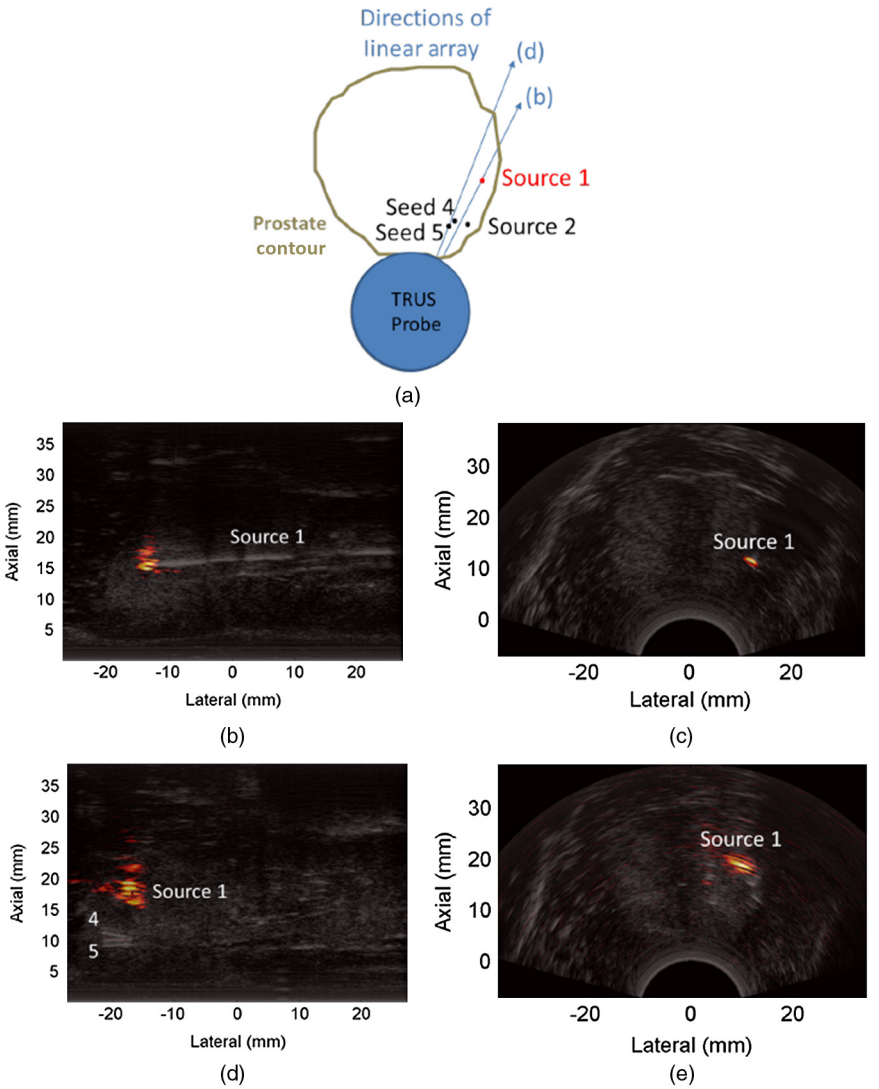

Fig. 6 (a) Schematic diagram of implanted seeds relative to the light source and TRUS probe with direction labels that correspond with the linear images in this figure. DAS photoacoustic images (overlaid on ultrasound B-mode images) showing fiber-related artifacts when the probe was placed to visualize the fiber tip (Source 1) with the (b) linear and (c) curvilinear arrays. Corresponding artifacts associated with Source 1 when the probe was (d) rotated and (e) translated away from the fiber tip. Source 2 was not yet inserted when these ultrasound and photoacoustic images were acquired.

tip in both linear and curvilinear images. A similar artifact was observed in the first dog (e.g., Fig. 2), when the fiber and sheath were translated together (not shown), and in our previous experiments with 10% gelatin.[23]

Although seeds #4 and 5 were not visualized in the photoacoustic image of Fig. 6(d), they were visualized when a second light source (Source 2) was placed closer to the seeds, as discussed in Sec. 3.5. The two sheaths corresponding to Sources 1 and 2 remained in place throughout the procedure and during postoperative CT image acquisitions.

3.4 *Echo Clutter*

To investigate the source of the high-amplitude artifact in Fig. 2(d), Source 1 acted as an echogenic reflector for the photoacoustic signals originating from Source 2. These two sources are illustrated in Fig. 7(a) relative to seed #1, which is located inferior to seeds #4 and 5 in Fig. 6(a). The cross sections of the two hollow sheaths appear as black dots in the CT image in Fig. 7(b). Seed #1 is located approximately 3 mm from Source 2 in this CT image. The fiber was inserted into Source 2 with the linear array directed toward this source, as indicated by the (c) in Fig. 7(a). The familiar fiber-related artifact was observed at the sheath tip with contrast, CNR, and SNR of 38 dB, 161, and 163, respectively, in the DAS image, as shown in Fig. 7(c).

Figure 7(d) shows the DAS image achieved when the ultrasound probe was rotated to visualize Source 1 with the fiber location unaltered and the linear array direction indicated by (d, e) in Fig. 7(a). The seed was visualized with respective contrast, CNR, and SNR of 13 dB, 8.5, and 11 in the DAS image and 6.6 dB, 1.5, and 0.9 in the SLSC image ($M = 1$, not shown). In addition, two artifacts appeared, one being the familiar diffuse fiber-related artifact with contrast, CNR, and SNR reduced to 67 dB, 139, and 139, respectively in the DAS image, compared to Fig. 7(c). The second artifact had respective contrast, CNR,

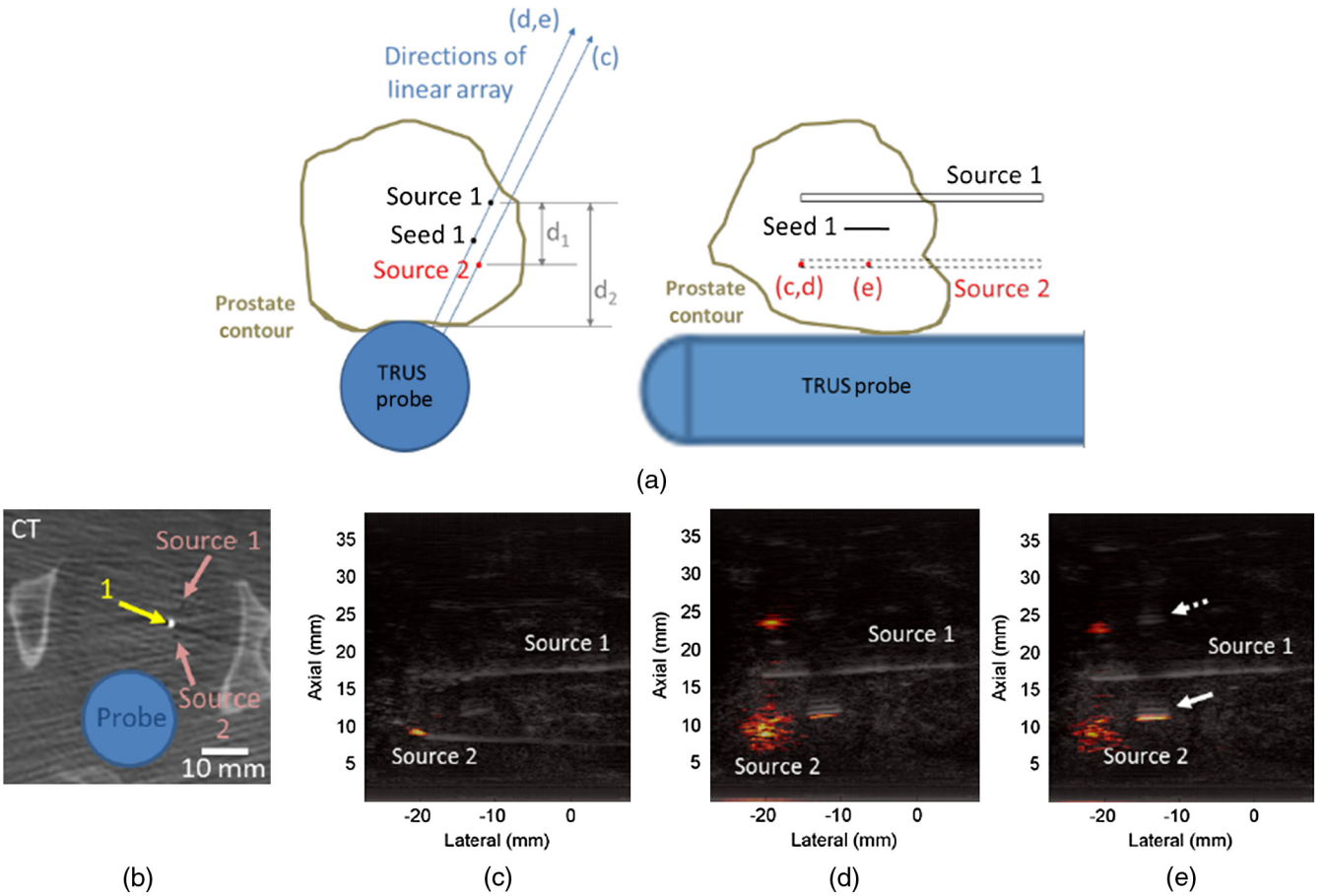

Fig. 7 (a) Schematic diagrams of implanted seeds relative to the TRUS probe with labels for the linear array directions and fiber tip that correspond with the labeled images in this figure. (b) CT image and DAS photoacoustic images of (c) the fiber tip, (d) a seed and two artifacts when the probe was rotated off-axis from the light source and (e) a seed and the two artifacts when the fiber was translated inside the sheath. The solid white arrows point to a seed inside the prostate, while the dashed white arrow points to a seed echo that appears outside of the prostate in the underlying B-mode image.

and SNR of 17 dB, 14, and 16, in the DAS image, but it is not present in Fig. 7(c) because its contrast is 10 dB below the amplitude of the fiber-related artifact. The location of the fiber tip in Figs. 7(c) and 7(d) is indicated by the red dot labeled (c, d) in Fig. 7(a).

The fiber was pulled 1 cm away from the sheath tip, as described in our previous publication,[23] where light from the fiber is diffused radially around the fiber tip as well as through the conical sheath tip. This fiber tip position is indicated by the red dot labeled (e) in Fig. 7(a). The resulting DAS image is shown in Fig. 7(e). The two artifacts had 2 to 7 dB, 3 to 10, and 3 to 12 lower contrast, CNR and SNR, respectively, than those in Fig. 7(d), and the seed was visible with 8 dB, 13.5, and 13 more contrast, CNR, and SNR, respectively, in the DAS image, compared to the seed in Fig. 7(d). These metrics for the seed were improved by 14.4 dB, 1.6, and 1.7, respectively, in the corresponding SLSC image ($M = 1$, not shown) compared to the SLSC image of the data displayed in Fig. 7(d). In addition, note that the ultrasound image contains a "seed" located outside of the prostate (dashed arrow) that appears to echo the true seed inside the prostate (solid arrow).

The point-like artifacts in Figs. 7 and 2 were not present with the transurethral light delivery method used to image the *ex vivo* prostate (Fig. 4). However, they are unlikely to be caused by an *in vivo* acoustic absorber, primarily because this artifact is located farther from the light source than the most distant seed in Fig. 2 (i.e., it experiences less fluence), yet it has up to seven times higher SNR than this seed, and the optical absorption in this region is unlikely to be seven times larger than that of metal and India ink.[18,30–32,35–37] In addition, the artifact appears in a similar relative orientation to seed reverberations in the ultrasound images of Figs. 2 and 7.

In Fig. 7, this artifact is likely caused by acoustic echoes from the fiber-related artifacts (i.e., clutter) that originated from Source 2, traveled to Source 1 ($d_1 = 7.2$ mm, as measured in the ultrasound image), which acted as an echogenic reflector that caused the signal to travel to the transducer ($d_2 = 16.4$ mm, as measured in the ultrasound image), for a total acoustic travel distance of approximately 23.6 mm (i.e., $d_1 + d_2$). The distance of this signal from the probe (23.5 mm) agrees with this acoustic propagation theory. Likewise, echoes that created the similar artifact in Fig. 2(c) potentially traveled from the light source to seed #2 then back to the ultrasound probe.

3.5 *Imaging Closely Spaced Seeds*

A schematic of seeds #2 and 3 implanted in the prostate of the second dog is shown in Fig. 8(a). The corresponding CT image

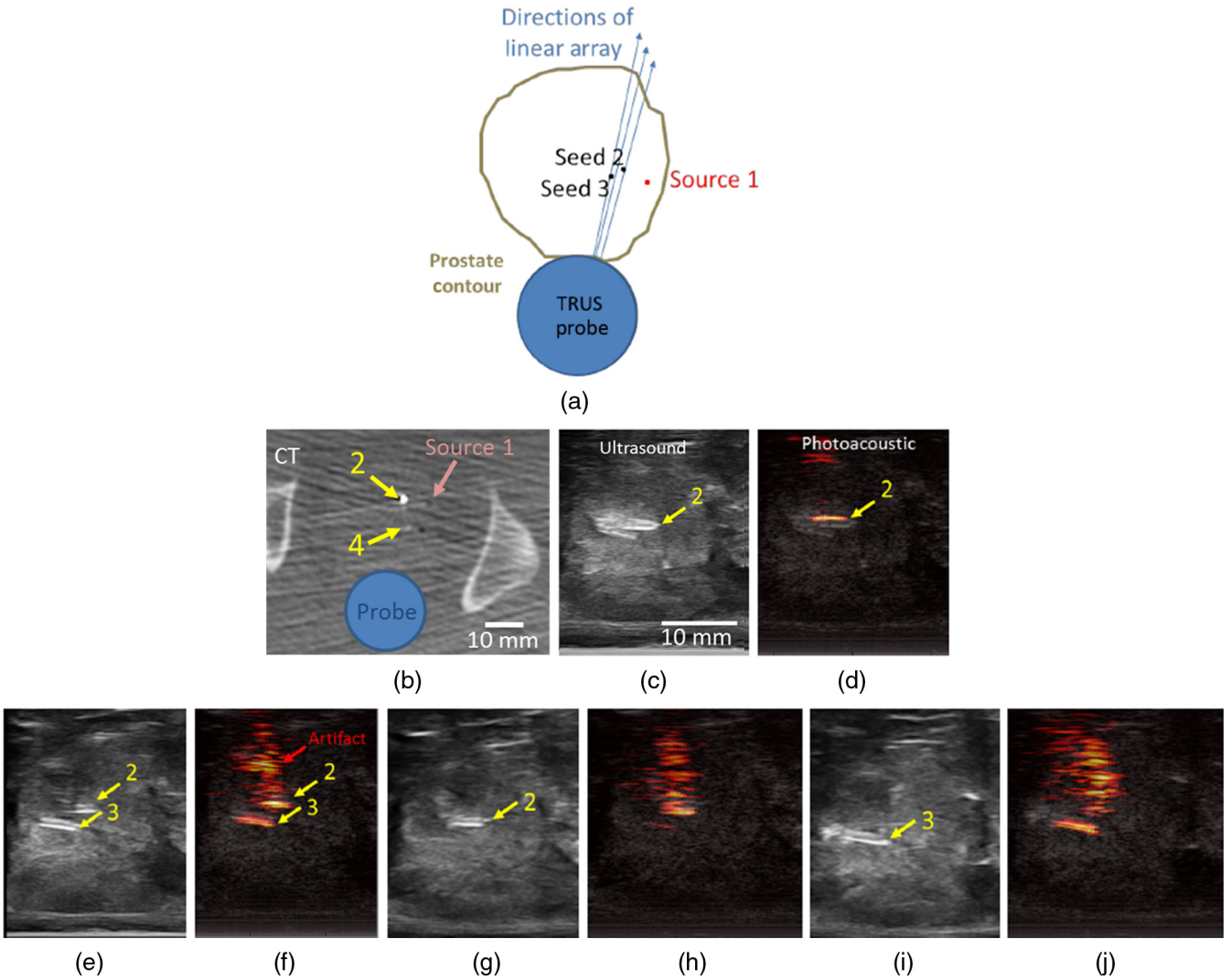

Fig. 8 (a) Schematic diagram of implanted seeds relative to the light source and TRUS probe with linear array directions that correspond to the ultrasound and photoacoustic images in this figure. (b) CT image showing seed #2 in relation to Source 1. (c) Ultrasound and (d) DAS photoacoustic images of seed #2 before other seeds were implanted. Respective ultrasound and DAS photoacoustic images (e, f) after seed #3 was implanted, (g, h) when seed #2 was isolated from seed #3 and (i, j) vice versa. Photoacoustic images were averaged over five frames.

is shown in Fig. 8(b), which highlights both seed #2 and the superior tip of seed #4. Seed #2 was implanted first, approximately 17 mm from the probe and 5 to 6 mm from Source 1. The ultrasound image of seed #2 before implantation of the remaining seeds is shown in Fig. 8(c). The corresponding photoacoustic image overlaid on the ultrasound image is shown in Fig. 8(d).

Seed #3 was implanted approximately 2 mm posterior to seed #2. The ultrasound image taken after seed #3 was implanted with the linear array directed toward both seeds is shown in Fig. 8(e). A corresponding photoacoustic image was acquired with the fiber location unaltered. Figure 8(f) shows the two seeds along with an artifact that was not present prior to the insertion of seed #3. Seeds #2 and 3 were each isolated in the ultrasound image plane by directing the linear array toward either seed as shown in Figs. 8(g) and 8(i), respectively. Photoacoustic imaging was performed and the corresponding images [Figs. 8(h) and 8(j), respectively] show a similar artifact.

These artifacts did not appear when a single seed was implanted nor when two seeds were implanted at least 4 mm apart (e.g., Fig. 2), and they had the same appearance when the imaging was repeated approximately 15 min later. In addition, similar artifacts were observed when the fiber was placed in Source 2 to visualize seeds #4 and 5 in Fig. 6, which were located 3 to 4 mm from this light source. These observations indicate that the artifacts were more likely caused by acoustic reverberations between the closely spaced seeds rather than *in vivo* chromophores.

4 Discussion

Brachytherapy seed detection with photoacoustic imaging depends on inherent optical and thermodynamic properties of brachytherapy seeds and the incident laser fluence. Generally, improving the ability of the DAS beamformer to detect implanted brachytherapy seeds (i.e., limited access to change seed properties) requires an increase in the incident laser fluence, which

Table 2 Summary of the light source, probe direction (linear and curvilinear arrays), approximate three-dimensional (3-D) light source-to-target distances measured from the fiber tip, energy densities, and coherent artifacts observed for each experiment.

Light source	Photoacoustic target and probe direction	3-D light source-to-target distance (mm)	Energy density at sheath tip (mJ/cm^2)	Coherent artifacts observed *in vivo*
Dog 1				
Interstitial (Fig. 2)	Seeds 1–3	5–9.5	84–167	Fiber, echo clutter
Urethra, end-firing fiber (Fig. 4)	Seeds 1–3	12	N/A	N/A
Dog 2				
Interstitial Source 1 (Fig. 6)	Tissue surrounding source 1	0–5	89	Fiber
Interstitial Source 2, fiber coincident with sheath tip [Fig. 7(c)]	Tissue surrounding source 2	0–5	89	Fiber, echo clutter
Interstitial Source 2, fiber coincident with sheath tip [Fig. 7(d)]	Seed 1 (linear array directed toward seed 1 and source 1)	11	89	Fiber, echo clutter
Interstitial Source 2, fiber pulled 1 cm from sheath tip [Fig. 7(e)]	Seed 1 (linear array directed toward seed 1 and source 1)	3	<89	Fiber, echo clutter
Interstitial Source 1 (Fig. 8)	Seeds 2 and/or 3	5–6	89	Reverberation between seeds
Interstitial Source 2 [Fig. 6(a)]	Seeds 4 and 5	3–4	89	Reverberation between seeds (image not shown)

raises safety concerns (e.g., exceeding the 100 mJ/cm^2 safety limit for skin exposure with a 1064-nm laser wavelength[43]). These concerns could be alleviated with geometry modifications (e.g., increase the conical tip slant height to increase the surface area) or considerations of the actual safety limit for prostates, which might be higher than that of skin.[18] SLSC beamforming is an alternative or supplemental approach to mitigate safety concerns, because it calculates the spatial coherence of the received acoustic wavefield and is, therefore, less susceptible to low laser fluence.[23] Results herein demonstrate that *in vivo* SLSC images have better contrast than *in vivo* DAS images for a combination of factors that cause low laser fluence (i.e., large distances between the target and light source and low laser energies).

Additional benefits of SLSC beamforming include visualization of out-of-plane seeds with similar contrast to that of in-plane seeds and superiority to image thresholding. These benefits are evident when low amplitude, spatially incoherent noise is reduced with the SLSC beamformer, while similarly low amplitude, spatially coherent seed signals (e.g., out-of-plane seeds) are preserved and displayed with similar amplitudes to in-plane seeds. *In vivo* application of this beamformer provided up to a 20-dB contrast improvement for the most distant seeds (e.g., seed #3 in Fig. 3). Larger improvements in contrast (i.e., 20 to 30 dB) were observed for an *in vivo* seed implanted 4 mm from the light source with energy densities at the fiber tip as low as 8 mJ/cm^2, which is 8% of the safety limit.[43] Similar improvements were achieved under the same conditions when the SLSC beamformer was compared with a conventional Fourier transform-based reconstruction method.[44,45] These improvements agree with our previous observations in phantoms and *ex vivo* tissue.[23]

Disadvantages of the SLSC beamformer include its inability to suppress spatially coherent artifacts and poor visualization of seeds located near a high-energy light source. The latter limitation is a result of the off-axis, coherent, high-amplitude fiber-related signals that add incoherently with the on-axis, lower-amplitude signals from the seeds, and reduce the spatial coherence of the seed signals. A similar effect was observed in SLSC ultrasound images.[24,25] The DAS beamformer does not suffer from this limitation, and the contrast was suitable for imaging seeds as close as 3 to 6.5 mm from the light source with energy densities of 108 to 167 mJ/cm^2 (Fig. 2) and 89 mJ/cm^2 (Fig. 7). In addition, the SNR is generally better in DAS images compared to SLSC images for a combination of large energies and small light source-to-target distances (i.e., high fluence incident on the seeds). Otherwise, the SNR of DAS and SLSC images are similar when both the light source-to-target distance and the laser energy are large (e.g., $\geq$1 cm and 95 to 163 mJ/cm^2, respectively) or small (e.g., 4 mm and 8 to 32 mJ/cm^2, respectively[44,45]), which both represent scenarios with low incident fluence.

Three artifacts (i.e., photoacoustic signals that are not seeds) present a challenge for interstitial light delivery and clinical translation to humans, as summarized in Table 2. One is a signal associated with optical absorption near the fiber tip, given the high fluence in this region. This artifact is likely caused by tissue, blood, or other endogenous chromophores located at the fiber tip, and it was also present in our previous phantom experiments.[23] Although it is an unwanted artifact, it can be regarded as an opportunity for intraoperative localization of the fiber tip. A second artifact originates from photoacoustic signals that encounter hyperechoic structures (i.e., echo clutter). In addition, multiple echo reverberation artifacts appear when seeds are closely spaced. Advanced shape-based filters may be applied to differentiate artifacts from seeds and to minimize potential false positives. A more detailed analysis of these artifact sources and potential reduction methods is beyond the scope of this paper.

Acoustic scattering in the canine prostate is expected to be similar to that of human prostates, while the similarity of optical properties at 1064-nm wavelength is not apparent based on the existing literature. At this wavelength, Nau et al.[36] reported that human prostates have higher absorption and more anisotropy than canine prostates, which disagrees with reports by Chen et al.[39] (630-nm wavelength) and Roggan et al.[46] (1064-nm wavelength), stating that the optical properties of normal canine prostates are similar to those of humans. However, the optical absorption and reduced scattering coefficient reported by Roggan et al.[46] differ by an order of magnitude from other reports at the same wavelength.[35–37] In spite of these discrepancies, the results herein provide some insights into the potential for clinical utility.

The proposed technique could be translated to humans by inserting multiple light diffusing sheaths in different regions of the prostate for the duration of a brachytherapy procedure. An optical fiber may then be inserted into any one of the sheaths and translated inside the sheath along the superior–inferior direction of the prostate (e.g., Fig. 7, which indicates that there is an optimal placement of the fiber with respect to the sheath and seeds). In addition, multiregional excitation might be achieved with simultaneous illumination through more than one sheath. Considering that seeds were visualized with pulse energies up to 10.5 mJ (i.e., 167 mJ/cm^2 for the current sheath geometry) at light source-to-target distances up to approximately 1 cm, and the prostate size spans 1.5 to 8 cm in the anterior–posterior and left–right directions,[47] at least 1 to 2 of these sheaths would be needed in each quadrant or hemisphere of the prostate for adequate seed illumination. However, one challenge is the echo clutter observed in Fig. 7, which might be overcome by inserting seeds farthest from the probe first, and then removing the echogenic HDR needles as seed implantation progresses toward the probe. An alternative is to mitigate this effect with side-firing transurethral light delivery through the urinary catheter that is routinely inserted during human procedures, which has potential to offer light directionality and selective seed illumination.[48]

Transperineal and transurethral laser irradiation of *in vivo* human prostates is commonly implemented in photodynamic therapy for prostate cancer, a treatment approach that requires preferential uptake of a photosenstitve drug and delivery of laser light to activate the drug and initiate cell death.[49–51] The current utilization of transperineal and transurethral light delivery in photodynamic therapy supports the clinical viability of these light delivery methods for photoacoustic imaging of prostate brachytherapy seeds.

5 Conclusion

For the first time, we demonstrate the *in vivo* feasibility of visualizing prostate brachytherapy seeds with photoacoustic imaging and evaluate the *in vivo* performance of the SLSC beamformer for this application. We utilized an interstitial transperineal light illumination method and a transrectal ultrasound probe. Co-registered ultrasound and photoacoustic images were acquired to confirm seed locations. Additional confirmation was provided with postoperative CT images of the implanted seeds and *ex vivo* validation. In addition, three artifacts related to the interstitial light delivery method were observed and preliminary investigations of their sources were presented. The *ex vivo* prostate results additionally highlighted the future potential for joint transurethral and transperineal light delivery methods. These contributions are significant in two aspects. First, they provide important steps toward clinical translation of promising tools for brachytherapy seed placement and interactive dosimetry adjustments. Second, the results are a major advance for photoacoustic imaging in general, as this is the first *in vivo* demonstration with an interstitial light delivery approach where the optics are separated from the acoustics, rather than integrated with the ultrasound probe.

Acknowledgments

M. A. Lediju Bell is a recipient of the Ford Foundation and UNCF/Merck Postdoctoral fellowships. Additional funding was provided by discretionary funds from the Johns Hopkins Department of Radiology and NIH under Grant Nos. CA180561 and EB015638.

References

1. P. Hoskin, "Prostate cancer: permanent low dose rate seed brachytherapy and temporary high dose rate afterloading brachytherapy," in *Proc. Radiotherapy in Practice-Brachytherapy*, p. 103 (2011).
2. J. Crook, "The role of brachytherapy in the definitive management of prostate cancer," *Cancer Radiothér.* **15**(3), 230–237 (2011).
3. J. C. Blasko et al., "Palladium-103 brachytherapy for prostate carcinoma," *Int. J. Radiat. Oncol. Biol. Phys.* **46**(4), 839–850 (2000).
4. J. C. Blasko et al., "The role of external beam radiotherapy with I-125/Pd-103 brachytherapy for prostate carcinoma," *Radiother. Oncol.* **57**(3), 273–278 (2000).
5. J. Crook et al., "10-year experience with I-125 prostate brachytherapy at the Princess Margaret Hospital: results for 1,100 patients," *Int. J. Radiat. Oncol. Biol. Phys.* **80**(5), 1323–1329 (2011).
6. M. J. Zelefsky et al., "Five-year outcome of intraoperative conformal permanent I-125 interstitial implantation for patients with clinically localized prostate cancer," *Int. J. Radiat. Oncol. Biol. Phys.* **67**(1), 65–70 (2007).
7. M. Buckstein et al., "Long-term outcomes and toxicity in patients treated with brachytherapy for prostate adenocarcinoma younger than 60 years of age at treatment with minimum 10 years of follow-up," *Urology* **81**(2), 364–369 (2013).
8. L. Potters, X. Wang, and Y. Yamada, "A nomogram to compensate for intraoperative prostate edema during transperineal brachytherapy." *Tech. Urol.* **6**(2), 99–103 (2000).
9. E. M. Messing et al., "Intraoperative optimized inverse planning for prostate brachytherapy: early experience," *Int. J. Radiat. Oncol. Biol. Phys.* **44**(4), 801–808 (1999).
10. S. Nag et al., "Intraoperative planning and evaluation of permanent prostate brachytherapy: report of the American Brachytherapy Society," *Int. J. Radiat. Oncol. Biol. Phys.* **51**(5), 1422–1430 (2001).
11. A. Polo et al., "Review of intraoperative imaging and planning techniques in permanent seed prostate brachytherapy," *Radiother. Oncol.* **94**(1), 12–23 (2010).
12. A. Sahgal and M. Roach, "Permanent prostate seed brachytherapy: a current perspective on the evolution of the technique and its application," *Nat. Clin. Pract. Urol.* **4**(12), 658–670 (2007).
13. S. Langley and R. Laing, "Prostate brachytherapy has come of age: a review of the technique and results," *BJU Int.* **89**(3), 241–249 (2002).
14. B. H. Han et al., "Prostate brachytherapy seed identification on post-implant TRUS images," *Med. Phys.* **30**, 898 (2003).
15. J. Mamou and E. J. Feleppa, "Singular spectrum analysis applied to ultrasonic detection and imaging of brachytherapy seeds," *J. Acoust. Soc. Am.* **121**(3), 1790–1801 (2007).
16. S. Nag et al., "The American Brachytherapy Society recommendations for permanent prostate brachytherapy postimplant dosimetric analysis," *Int. J. Radiat. Oncol. Biol. Phys.* **46**(1), 221–230 (2000).
17. T. Harrison and R. J. Zemp, "Coregistered photoacoustic-ultrasound imaging applied to brachytherapy," *J. Biomed. Opt.* **16**(8), 080502 (2011).
18. J. L. Su et al., "Photoacoustic imaging of prostate brachytherapy seeds," *Biomed. Opt. Express* **2**(8), 2243 (2011).

19. E. M. Boctor et al., "Prostate brachytherapy seed localization using combined photoacoustic and ultrasound imaging," presented at *Ultrasonic Imaging, Tomography and Therapy Medical Imaging*, Paper 7629-29, SPIE, San Diego, CA (14 February 2010).
20. M. Xu and L. V. Wang, "Photoacoustic imaging in biomedicine," *Rev. Sci. Instrum.* **77**(4), 041101 (2006).
21. N. Kuo et al., "Real-time photoacoustic imaging of prostate brachytherapy seeds using a clinical ultrasound system," *J. Biomed. Opt.* **17**(6), 066005 (2012).
22. L. Pan et al., "Improving photoacoustic imaging contrast of brachytherapy seeds," *Proc. SPIE* **8581**, 85814B (2013).
23. M. A. Lediju Bell et al., "Short-lag spatial coherence beamforming of photoacoustic images for enhanced visualization of prostate brachytherapy seeds," *Biomed. Opt. Express* **4**(10), 1964 (2013).
24. M. A. Lediju et al., "Short-lag spatial coherence of backscattered echoes: imaging characteristics," *IEEE Trans. Ultrason. Ferroelectr. Freq. Control* **58**(7), 1337 (2011).
25. M. A. Lediju Bell et al., "Short-lag spatial coherence imaging of cardiac ultrasound data: initial clinical results," *Ultrasound Med. Biol.* **39**(10), 1861–1874 (2013).
26. J. J. Dahl et al., "Lesion detectability in diagnostic ultrasound with short-lag spatial coherence imaging." *Ultrason. Imagaing* **33**(2), 119 (2011).
27. B. Pourebrahimi et al., "Improving the quality of photoacoustic images using the short-lag spatial coherence imaging technique," *Proc. SPIE* **8581**, 858141 (2013).
28. M. A. Lediju Bell et al., "Feasibility of transcranial photoacoustic imaging for interventional guidance of endonasal surgeries," *Proc. SPIE* **8943**, 894307 (2014).
29. H. O. Badwan et al., "AnchorSeed for the reduction of source movement in prostate brachytherapy with the Mick applicator implant technique," *Brachytherapy* **9**(1), 23–26 (2010).
30. J. Su et al., "Photoacoustic imaging of clinical metal needles in tissue," *J. Biomed. Opt.* **15**(2), 021309 (2010).
31. T. Mitcham et al., "Modulation of photoacoustic signal generation from metallic surfaces," *J. Biomed. Opt.* **18**(5), 056008 (2013).
32. A. Krainov et al., "Optical properties of mouse biotissues and their optical phantoms," *Opt. Spectrosc.* **115**(2), 193–200 (2013).
33. H. G. Craighead and A. Glass, "Optical absorption of small metal particles with adsorbed dye coats," *Opt. Lett.* **6**(5), 248–250 (1981).
34. N. Kometani et al., "Preparation and optical absorption spectra of dye-coated Au, Ag, and Au/Ag colloidal nanoparticles in aqueous solutions and in alternate assemblies," *Langmuir* **17**(3), 578–580 (2001).
35. S. Chitchian and N. M. Fried, "Near-IR optical properties of canine prostate tissue using oblique-incidence reflectometry," *Proc. SPIE* **7548**, 75480Z (2010).
36. W. H. Nau, R. J. Roselli, and D. F. Milam, "Measurement of thermal effects on the optical properties of prostate tissue at wavelengths of 1,064 and 633 nm," *Lasers Surg. Med.* **24**(1), 38–47 (1999).
37. A. A. Oraevsky, S. L. Jacques, and F. K. Tittel, "Measurement of tissue optical properties by time-resolved detection of laser-induced transient stress," *Appl. Opt.* **36**(1), 402–415 (1997).
38. S. Rastegar et al., "Theoretical analysis of equivalency of high-power diode laser (810 nm) and Nd: YAG laser (1064 nm) for coagulation of tissue: predictions for prostate coagulation," *Proc. SPIE* **1646**, 150–160 (1992).
39. Q. Chen et al., "Changes in in vivo optical properties and light distributions in normal canine prostate during photodynamic therapy," *Radiat. Res.* **147**(1), 86–91 (1997).
40. M. A. Lediju Bell et al., "In vivo reproducibility of robotic probe placement for a novel ultrasound-guided radiation therapy system," *J. Med. Imaging* **1**(2), 025001 (2014).
41. R. J. Fedewa et al., "Spatial coherence of the nonlinearly generated second harmonic portion of backscatter for a clinical imaging system," *IEEE Trans. Ultrason. Ferroelectr. Freq. Control* **50**(8), 1010–1022 (2003).
42. M. D. Abràmoff, P. J. Magalhães, and S. J. Ram, "Image processing with imageJ," *Biophoton. Int.* **11**(7), 36–43 (2004).
43. A. Standard, *Z136. 1. American National Standard for the Safe Use of Lasers*, American National Standards Institute, Inc., New York (1993).
44. M. A. Lediju Bell, D. Y. Song, and E. M. Boctor, "Coherence-based photoacoustic imaging of brachytherapy seeds implanted in a canine prostate," *Proc. SPIE* **9040**, 90400Q (2014).
45. M. A. Lediju Bell et al., "In vivo photoacoustic imaging of prostate brachytherapy seeds," *Proc. SPIE* **8943**, 894348 (2014).
46. A. Roggan et al., "Experimental set-up and Monte-Carlo model for the determination of optical tissue properties in the wavelength range 330 to 1100 nm," *Proc. SPIE* **2323**, 21–36 (1995).
47. C. G. Roehrborn et al., "Correlation between prostate size estimated by digital rectal examination and measured by transrectal ultrasound," *Urology* **49**(4), 548–557 (1997).
48. M. A. Lediju Bell et al., "Photoacoustic imaging of prostate brachytherapy seeds with transurethral light delivery," *Proc. SPIE* **8943**, 89430N (2014).
49. T. C. Zhu, J. C. Finlay, and S. M. Hahn, "Determination of the distribution of light, optical properties, drug concentration, and tissue oxygenation in-vivo in human prostate during motexafin lutetium-mediated photodynamic therapy," *J. Photochem. Photobiol. B: Biol.* **79**(3), 231–241 (2005).
50. T. R. Nathan et al., "Photodynamic therapy for prostate cancer recurrence after radiotherapy: a phase I study," *J. Urol.* **168**(4), 1427–1432 (2002).
51. C. M. Moore, D. Pendse, and M. Emberton, "Photodynamic therapy for prostate cancera review of current status and future promise," *Nat. Clin. Pract. Urol.* **6**(1), 18–30 (2009).

Muyinatu A. Lediju Bell is a postdoctoral fellow at Johns Hopkins University. She completed her PhD degree in biomedical engineering at Duke University in 2012 and received her BS degree in mechanical engineering from the Massachusetts Institute of Technology in 2006. Her research interests include ultrasound and photoacoustic image quality improvements, acoustic wave propagation theories, and clinical translation of novel medical imaging technologies that improve the standard of cancer patient care.

Nathanael P. Kuo is a postdoctoral fellow in the Department of Electrical and Computer Engineering at Johns Hopkins University. He obtained his PhD degree in biomedical engineering from Johns Hopkins University and his BS degree in electrical engineering from the University of Illinois at Urbana-Champaign with minors in computer science and mathematics. Currently, he specializes in ultrasound medical image analysis for image-guided therapy within the broader field of medical imaging.

Danny Y. Song serves as the clinical director and director of brachytherapy in the Department of Radiation Oncology and Molecular Radiation Sciences at Johns Hopkins University School of Medicine. His research focus is on technological innovations and image guidance for improving the practice of prostate radiotherapy, as well as clinical research in radiotherapy for prostate cancer and other genitourinary malignancies.

Jin U. Kang is the Jacob Suter Jammer Professor of Electrical and Computer Engineering, Johns Hopkins University. His research interests include the areas of biophotonics, three-dimensional (3-D) OCT intraoperative imaging (Real-Time OCT), smart surgical tools, and fiber optic devices and sensors.

Emad M. Boctor is an assistant professor in the Departments of Radiology and Computer Science at Johns Hopkins University. His interests encompass medical imaging, ultrasound instrumentation, elasticity/thermal/photoacoustic imaging, image-guided intervention, and robotics.